Electrical unfolding of cytochrome *c* during translocation through a nanopore constriction

Prabhat Tripathi[a], Abdelkrim Benabbas[a], Behzad Mehrafrooz[b], Hirohito Yamazaki[a], Aleksei Aksimentiev[b,c], Paul M. Champion[a,d,1], and Meni Wanunu[a,d,1]

[a]Department of Physics, Northeastern University, Boston, MA 02115; [b]Center for Biophysics and Quatitative Biology, University of Illinois at Urbana–Champaign, Urbana, IL 61801; [c]Department of Physics and Beckman Institute for Advanced Science and Technology, University of Illinois at Urbana–Champaign, Urbana, IL 61801; and [d]Center for Interdisciplinary Research on Complex Systems, Northeastern University, Boston, MA 02115

Edited by William A. Eaton, National Institute of Diabetes and Digestive and Kidney Diseases, Bethesda, MD, and approved March 13, 2021 (received for review July 31, 2020)

Many small proteins move across cellular compartments through narrow pores. In order to thread a protein through a constriction, free energy must be overcome to either deform or completely unfold the protein. In principle, the diameter of the pore, along with the effective driving force for unfolding the protein, as well as its barrier to translocation, should be critical factors that govern whether the process proceeds via squeezing, unfolding/threading, or both. To probe this for a well-established protein system, we studied the electric-field–driven translocation behavior of cytochrome *c* (cyt *c*) through ultrathin silicon nitride (SiN_x) solid-state nanopores of diameters ranging from 1.5 to 5.5 nm. For a 2.5-nm-diameter pore, we find that, in a threshold electric-field regime of ∼30 to 100 MV/m, cyt *c* is able to squeeze through the pore. As electric fields inside the pore are increased, the unfolded state of cyt *c* is thermodynamically stabilized, facilitating its translocation. In contrast, for 1.5- and 2.0-nm-diameter pores, translocation occurs only by threading of the fully unfolded protein after it transitions through a higher energy unfolding intermediate state at the mouth of the pore. The relative energies between the metastable, intermediate, and unfolded protein states are extracted using a simple thermodynamic model that is dictated by the relatively slow (∼ms) protein translocation times for passing through the nanopore. These experiments map the various modes of protein translocation through a constriction, which opens avenues for exploring protein folding structures, internal contacts, and electric-field–induced deformability.

nanopore biophysics | cytochrome *c* | protein folding | electric field unfolding | solid-state nanopore

Protein unfolding during its translocation through a nanoconstriction, and its subsequent refolding after translocation, are two ubiquitous processes in biology (1–6). In order to fully understand the two processes, a plethora of experiments that use nanopores as mimics of a real biological constriction have been performed (7–24). In these studies, voltage applied across a pore electrokinetically pulls a protein into and subsequentially through it. These studies are also critical to overcoming technical challenges associated with protein sequencing using nanopores, where tertiary and secondary structures must be unfolded to allow single-file threading of a protein through the nanopore sensor. Interactions of partially and fully unfolded proteins with biological and solid-state pores in the presence of chemical denaturants have been studied extensively (7–10). The use of an enzymatic motor to achieve processive threading of unfolded proteins was demonstrated recently (11). In other pioneering experiments, electric-field–driven unidirectional threading was demonstrated by tagging the end terminal of the model protein thioredoxin with an oligonucleotide (12, 13). In these studies, the size of the pore was smaller than that of a fully folded protein ($d_{pore} < d_{protein}$) and translocation of protein necessarily required denaturing agents, an enzyme, or an oligo tag. Nanopores with larger diameters than the folded protein ($d_{pore} > d_{protein}$) were also employed (8, 14–22), and due to the extremely fast translocation times of folded protein transport, only a tiny fraction of the translocated population was detected (14, 15, 17, 19), predominantly the longer events associated with protein sticking to the pore walls (15, 19). Slowing protein translocation by tethering to a lipid coating on the pore walls achieved orders of magnitude reduction in the translocation times and allowed efficient protein detection (18). High-bandwidth measurements combined with the use of "tighter" pore diameters have been used to capture the fast translocation events of folded proteins and further utilized to estimate size (16, 20, 25), conformation (21), and conformational flexibility (22).

Here, we report that a fully folded heme protein cytochrome *c* (cyt *c*, Fig. 1*A*) can pass through an ultrathin solid-state nanopore ($d_{pore} < d_{protein}$) and translocate without requiring chemical denaturants, an unfolding enzyme, or an oligonucleotide tag. Instead, protein unfolding during translocation can be achieved by controlling the electric field across the pore. We report how solid-state nanopores can unfold a protein during its translocation through a nanoconstriction that is smaller than the protein diameter. The nanoconstriction allows studying the protein in a "trapped" mode where the native state of the protein is not allowed to pass through, but partial unfolding and reequilibration of the protein can take place at the pore. This leads to an outcome where unfolding of the remaining secondary α-helical structure can be induced by an electric field during translocation.

Significance

Can localized electric fields drive the complete unfolding of a protein molecule? Protein unfolding prior to its translocation through a nanopore constriction is an important step in protein transport across biological membranes and also an important step in nanopore-based protein sequencing. We studied here the electric-field–driven translocation behavior of a model protein (cyt *c*) through nanopores of diameters ranging from 1.5 to 5.5 nm. These single-molecule measurements show that electric fields at the nanopore constriction can select both partially and fully unfolded protein conformations. Zero-field free energy gaps between these conformations, found using a simple thermodynamic model, are in remarkable agreement with previously reported studies of cyt *c* unfolding energetics.

Author contributions: P.T., A.B., B.M., A.A., P.M.C., and M.W. designed research; P.T., B.M., and H.Y. performed research; P.T., A.B., B.M., A.A., and P.M.C. analyzed data; and P.T., A.A., P.M.C., and M.W. wrote the paper.

The authors declare no competing interest.

This article is a PNAS Direct Submission.

[1]To whom correspondence may be addressed. Email: p.champion@northeastern.edu or wanunu@neu.edu.

This article contains supporting information online at https://www.pnas.org/lookup/suppl/doi:10.1073/pnas.2016262118/-/DCSupplemental.

Published April 21, 2021.

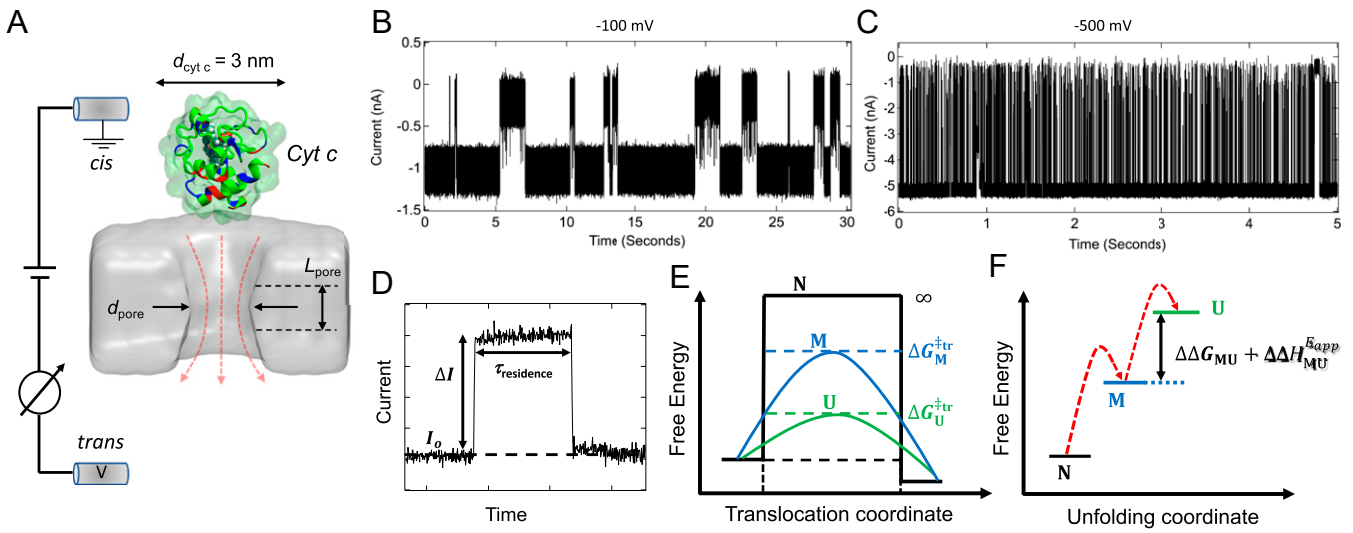

Fig. 1. Cyt *c* squeezing/unfolding through a solid-state silicon nitride nanopore. (*A*) Schematic of our experimental setup; application of a negative voltage to the trans chamber electrokinetically captures cyt *c* molecules at the pore vicinity. (*B* and *C*) Representative ionic current recordings for a d_{pore} = 2.5 nm (L_{pore} = 3.4 nm), in 1 M KCl, 10 mM Hepes, pH 7.5 buffer at −100 mV (*B*) and at −500 mV (*C*), respectively. (*D*) Description of the parameters in a typical current blockade event. (*E*) Schematic energy diagram for translocation of cyt *c*. In the native state (N), the energy barrier for protein translocation through the pore is assumed to be pseudoinfinity due to steric constraints, whereas the energy barrier of a partially unfolded metastable squeezed state (M), which still has intact α-helices, remains relatively large compared to the completely unfolded state, U. Due to interaction with an external electric field and fast α-helical conformational transitions, the low-barrier U-state population increases leading to larger average translocation rates. (*F*) The conformational populations of the protein are governed by thermal excitations, the zero-field free energy gap between conformations ($\Delta\Delta G_{MU}$), and the effect of the external electric field $\left(\Delta\Delta H_{MU}^{E_{app}}\right)$.

Although this experiment is fundamentally different from DNA unzipping (26–28), stretching (29), and translocation (30), there are certain similar outcomes in the analysis. For example, we observed that there is a voltage or electric-field threshold to observe transitions in the protein conformation, and we find that the translocation rate is conformation dependent.

Cyt *c* Interaction with a Nanopore

We chose cyt *c* as our model protein (*SI Appendix*, section 2 and Fig. S1, *i* and *ii*) because of ample investigations concerning the energetics of its conformationally excited metastable and unfolded states (31–33). In its native state, cyt *c* is relatively small (MW = 12 kDa, $d_{protein}$ ~3 nm), positively charged (+8 at physiological pH), its structure can be modulated under the action of electric field (34), and it can translocate through mitochondrial pores (6, 35, 36) and other small constrictions (37) (d_{pore} < 3 nm). Moreover, some conformational changes of cyt *c* are known to involve the removal of the Met-80 heme ligand (38–42). These conformational changes are known to be functionally relevant; for example, upon interaction with the mitochondrial membrane, cyt *c* loses the Met-80 heme ligand and transitions from an electron transport protein to a peroxidase, initiating the process of apoptosis (43–46).

Earlier studies on cyt *c* reported that the energy required to unfold cyt *c* is > 21.6 k_BT_0 (12.8 kcal/mol with T_0 = 298 K) (32), a significantly high energy (> 500 meV) to achieve on a lipid-supported biological nanopore platform, even at maximally supported voltages of up to 350 mV (47). In contrast, solid-state nanopores allow us to perform experiments at high voltage (~1 V) and also robustly analyze the same molecule with different pore diameters while maintaining the electrostatic and hydrophobic environment of the inner pore lumen (48–50). The arrangement of a solid-state nanopore within the flow cell is shown in Fig. 1*A* where a negative potential is applied to the trans compartment. The resulting steady-state ion current is transiently interrupted only by cyt *c* molecules interacting with the pore. The electric-field intensity is maximum inside the pore and decays rapidly outside the pore entrance (29, 50). The positively charged cyt *c* is captured at the pore entrance via a drift-diffusion mechanism (24, 50), and following its trapping at the pore mouth, depending upon the applied potential, it can either undergo conformational transitions and translocate through the pore or escape back to the cis compartment. Given the dipolar nature of cyt *c*, we expect that in the applied voltage regime used here, the resulting electric field in the pore vicinity can preferentially orient and separate the differentially charged segments of cyt *c* prior to its translocation (*SI Appendix*, section 5). The orientation-dependent energetics of the protein, due to permanent and induced dipole interactions with the electric field (and its gradient) are, for simplicity, treated here using scalar fitting parameters. We also emphasize that rapid timescale (0.1 to 10 μs) α-helical unfolding/folding processes (51–56) are key aspects of the secondary structure of cyt *c* and that these relatively fast conformational transitions appear to govern the much slower (~ms) translocation of the protein through pores with diameters of 2.0 to 2.5 nm.

Example traces at −100 and −500 mV are shown in Fig. 1 *B* and *C*, respectively (for other voltages reference *SI Appendix*, section 6 and Fig. S3, *i–vii*). A single interaction of a protein molecule with the pore, shown in Fig. 1*D*, can be characterized by a reduction in the open pore current (I_o) by some amplitude (ΔI), as well as by the duration of this interaction time ($\tau_{residence}$). As can be discerned from previous work (19, 57), as well as from the molecular-dynamics (MD) simulations presented below, the scaleless fractional blockade $\Delta I/I_o$ provides information about the nature of the protein occupancy in the pore (e.g., squeezed, stretched, or unfolded), while the value of $\tau_{residence}$ provides information about the rate of protein translocation and its associated free energy barrier. We reason that translocation for d_{pore} < $d_{protein}$ requires excitation of the native protein, N, to higher energy, partially unfolded, conformations. Thus, in addition to N, we consider a metastable squeezed state, M, a fully

unfolded state, U, and an intermediate state, I, on the pathway between M and U. The residual α-helical secondary structures associated with the M and I states are described in more detail below. As the electric field increases, these states can interconvert, either in the nanopore or at the mouth of the pore, making the protein more flexible and reducing both the fractional blockade ($\Delta I/I_o$) and the energetic barrier to translocation, $\Delta G^{\ddagger tr}$.

Thermodynamic Model

In the studies reported here, translocation of cyt *c* through a 2.5-nm pore takes place on (~ms) timescales. This means that protein secondary structures that reequilibrate on much faster ($\lesssim 10$ μs) timescales can be considered within a thermodynamic quasi-equilibrium framework (i.e., using a preequilibrium kinetic assumption). The thermodynamic analysis describes the translocation process under near-equilibrium conditions for the α-helix state transitions, while the MD simulations described below probe highly nonequilibrium transport on ~ns timescales. This two-pronged approach allows us to consider the nonequilibrium processes that are likely to occur, even on the experimentally observed (~ms) translocation timescale, as well as to analyze the thermally driven conformational reequilibration processes that are constantly taking place on much faster timescales.

As an example, in Fig. 1*E*, we illustrate the energy diagram for translocation within a pore that denies access to the N state but allows entrance and "squeezing" of a partially unfolded M state, which has the three residual α-helices of cyt *c* intact (32, 58, 59). For smaller pores, which do not allow access to M, conformational excitations due to the electric field at the mouth of the pore can still take place and affect the ion current. Thus, for the experiments using a 2.0-nm-diameter pore described below, a two-state analysis was used to describe interconversions between M and an intermediate I state, which lies on the pathway to U, where one of the α-helices has unfolded (32, 58, 59). In a larger 2.5-nm pore, where the M state of cyt *c* can enter by squeezing, both two-state ($M \leftrightarrow U$) and three-state ($M \leftrightarrow I \leftrightarrow U$) models were used for analysis. These models are discussed in more detail in *SI Appendix*, sections 7 and 15. In both models, a flexible dynamically interconverting thermodynamic state mixture, associated with rapid (51–56) α-helix folding/unfolding transitions, facilitates translocation through the pore and affects the observed fractional blockades.

The conformational excitation of an electrically polarized (or polarizable) protein to a state of higher electric dipole moment can be induced by the action of an applied electric field. This occurs because the applied field reduces the energy gap between conformational states with differing net dipole moments. As an example, using just the two states M and U (in addition to N), we depict in Fig. 1*F* an inherent zero-field free energy gap, $\Delta\Delta G_{MU}$, that is reduced by a field-dependent interaction energy. The field dependence of the energy gap is defined as follows: $\Delta\Delta H_{MU}^{E_{app}} = \Delta H_{NU}^{E_{app}} - \Delta H_{NM}^{E_{app}}$. More specifically, the electric-field–dependent energy gap between the states M and U can be written as follows:

$$\Delta\Delta H_{MU}^{E_{app}} = -\Delta p_{MU} E_{app} - \frac{1}{2}\Delta\alpha_{MU} E_{app}^2. \quad [1]$$

Here, $\Delta p_{MU} = p_U - p_M$ and $\Delta\alpha_{MU} = \alpha_U - \alpha_M$ are taken to be positive fitting parameters that include dipole-field orientation as well as any associated dielectrophoretic effects (29) where the gradient is expanded in powers of applied field. The field primarily interacts with either the permanent dipole moment (p_M and p_U) of each state or with the conformation-dependent induced dipoles (34) that depend on both the polarizability and the applied field (i.e., $\alpha_M E_{app}$ and $\alpha_U E_{app}$). As the electric field is increased, we expect the dipoles to orient along the field so that $p_U > p_M$ and $\alpha_U E_{app} > \alpha_M E_{app}$, due to the protein elongation (and the charges within it) in the U-state conformation. Under this condition, the potential energy level associated with U will decrease relative to M as the magnitude of the field increases.

Thus, as the applied field increases, an energy-level degeneracy occurs, where the thermodynamic population probabilities of M and U become equal, and M is no longer a thermodynamically stabilized state. The resulting rapid (0.1 to 1 μs) timescale (51–56) thermodynamic α-helix unfolding/folding leads to a population mixture between M and U that affects the fractional blockade. It also facilitates translocation through the pore but on much slower (ms) timescales than the underlying α-helix interconversion times. At still higher fields, level inversion takes place, and the unfolded conformation (U) becomes more thermodynamically stable than M. If only one of the three α-helices unfolds (32, 58, 59), a sequential intermediate state, I, should be included in the thermodynamic analysis. Finally, we note that, so long as the timescale separation that allows thermodynamic averaging is maintained, we do not need to explicitly consider the frictional forces that might affect the transition rates between the folded and unfolded α-helices linking the M, I, and U states.

Results and Analysis

We present here extensive measurements of the fractional change in current amplitudes and residence times for many single-molecule passage events of cyt *c* through various solid-state pores under native and denaturing conditions. These experiments shed light on the kinetics and energetics of cyt *c* translocation by using a statistical analysis of the molecular ensemble. We use the thermodynamic model to analyze the electric-field–dependent fractional blockades and, for the 2.5-nm pore, we extract the zero-field free energy gap, $\Delta\Delta G_{MU} = \Delta G_{NU} - \Delta G_{NM}$. The results from the 2.0-nm pore also allow $\Delta\Delta G_{MI}$ to be found. Thus, by use of both the pore size and the external electric field, the relative energies of different partially folded conformations of cyt *c* can be probed. As described below, the zero-field free energy gaps obtained with this single-molecule nanopore technique are in remarkable agreement with prior studies of cyt *c* unfolding energetics (32, 58). Finally, the zero-field translocation energy barriers for the M state ($\Delta G_M^{\ddagger tr}$), U state ($\Delta G_U^{\ddagger tr}$), and I state ($\Delta G_I^{\ddagger tr}$) can also be estimated from the residence time (kinetic) measurements.

Smaller Pore Imposes a Free Energy Barrier during cyt *c* Translocation. Scatter plots of fractional blockades versus residence times for different pore diameters are shown in Fig. 2*A*. Example traces for different pore diameters are shown in *SI Appendix*, section 8 and Fig. S4. For the 5.5-nm pore (V = 100 mV), we observe short-lived events (~200 μs) with relatively shallow fractional blockades (~0.36). Decreasing the pore size to 3.5 nm resulted in similar event durations (~120 μs) yet deeper fractional blockades (~0.8), as expected. Further decreasing the pore diameters to 3.0 and 2.5 nm increased the fractional blockades to near unity and greatly increased event durations to 10 to 100 ms, orders of magnitude greater than for the larger pore sizes. Moreover, in the experiments with 3.0- and 2.5-nm pores, higher voltages were required to observe translocation events than for the larger pores. Given the molecular dimensions of cyt *c*, these results suggest that decreasing the pore diameter to below 3 nm imposes a significant free energy barrier for cyt *c* translocation in its native state; that is, conformational excitation is required for the protein to move through the pore.

Threading of the Unfolded Protein after a Transition at the Mouth of the 2.0-nm-Diameter Pore. As the pore size is further reduced, we observe increases in the magnitude of the translocation barrier. In Fig. 2*B*–*F*, we present results for a 2.0-nm-diameter pore. A representative distribution of fractional blockades obtained for the 2.0-nm pore is shown in Fig. 2*B*. Since we observed two

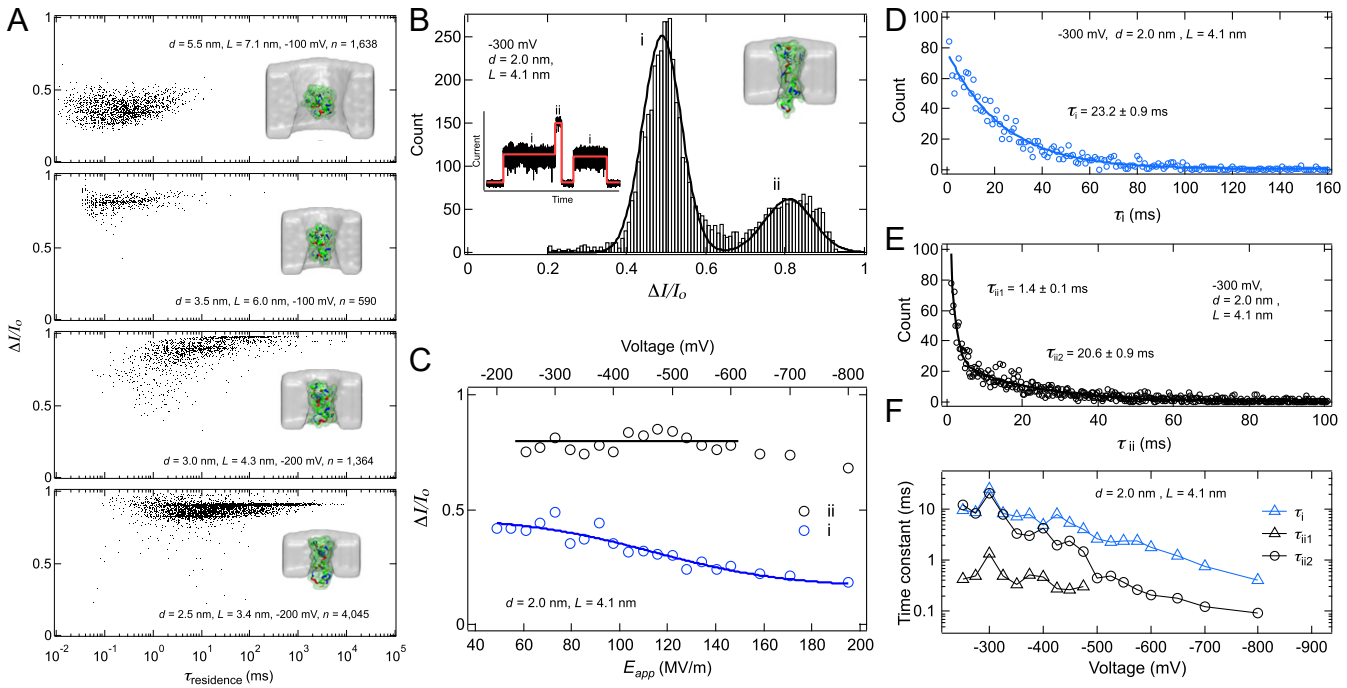

Fig. 2. Conformationally excited states of cyt *c* during translocation. (*A*) Scatter plots of fractional current blockades and residence times for different pore dimensions. (*Insets*) Snapshots from all-atom MD simulations. (*B*) Current blockade distribution for cyt *c* in a 2.0-nm pore (full scatter plots are found in *SI Appendix*, section 21) shows two distinct populations of blockade events. The black curve represents a double Gaussian fit. (*Inset*) Example multilevel events and two-level fits (red curve) reveal levels i and ii. (*C*) Voltage dependence of mean fractional blockades for levels i and ii. Level ii is nearly independent of voltage, whereas level i decreases with voltage. The blue curve is a fit using the two-state model described by Eq. **2**, where the M and I state are interconverting at the mouth of the pore, prior to a transition to the U state and threading into the pore. Fit parameters are given in Table 1. (*D–F*) Distribution of the level i lifetime with a single-exponential fit for τ_i (blue curve), distribution of the level ii lifetime with a double-exponential fit for τ_{ii1} and τ_{ii2} (black curve), and voltage dependence of time constants τ_i, τ_{ii1}, and τ_{ii2}, respectively.

characteristic levels (i and ii) produced by the protein, which often occur in succession (i → ii for the same molecule, see Fig. 2*B*, *Inset trace*), we decoupled the two states by using a custom script to independently quantify the durations and blockade levels for each of these states (*SI Appendix*, section 1). Based on these observations, we assigned level i to protein docking at the pore mouth where it attempts (but fails) to squeeze through the pore via the partially unfolded M state, which retains its full α-helical content. Instead of squeezing, the M state begins to undergo transitions with another unfolding intermediate (I state, where the shortest of the three cyt *c* α-helices is unfolded) at the mouth of the pore. Further α-helical unfolding results in the U state, which either escapes back to the cis chamber or threads deeper into the pore leading to blockage level ii. Similar event shapes (i → ii) were observed for a 1.5-nm-diameter pore at −500 mV (*SI Appendix*, section 9 and Fig. S5 *A* and *B*).

In additional studies, we did not observe a substantial number of events with level ii at voltages weaker than −250 mV, indicating that there is a significant voltage threshold necessary to fully unfold cyt *c* so that it is able to enter the 2.0-nm pore constriction. As higher voltages were applied, the number of level ii events increased up to about −400 mV and then leveled off (*SI Appendix*, section 10 and Fig. S6). Furthermore, whereas the $\Delta I/I_o$ peak position of level ii (Fig. 2*C*) remains constant as a function of voltage in the range −250 mV < V < −650 mV, we find that the i blockade level systematically decreases with stronger applied voltage. This behavior stands in contrast to DNA unzipping (26–28) and translocation experiments (30), where fractional blockades do not change with the voltage. We attribute this behavior (Fig. 2*C*, blue curve) to electric-field–induced transitions of cyt *c* between the partially unfolded metastable M state and the more unfolded state, I, which leads to more ion permeation depending on the field-dependent relative population of the M and I states. When the protein fully unfolds to U, the level ii blockade ratio is established because the protein is now finally able to enter into the 2.0-nm pore where it blocks the ion current.

We assign the formation of the cyt *c* M state to electric-field–induced breakage of the salt bridge involving E62, which subsequently releases residues 40 to 57 within an Ω-loop region (59). Because the applied field should also lead to dissociation of Met80 (34), the unfolding of its associated Ω-loop residues 70 to 87 is also assumed to take place. Thus, we suggest that the action of the electric field at the entrance to the nanopore can induce the lowest energy unfolding transitions of cyt *c* (32, 58). This produces the smaller and more compressible M state, which is chiefly composed of the three primary α-helices of cyt *c*. Because these helices are energetically stabilized, they are more difficult to unfold (32, 58). Based on prior work (32, 58), the I state is presumed to involve the unfolding of the short α-helix associated with residues 61 to 69.

The blue curve in Fig. 2*C* is a simple two-state fit (*SI Appendix*, section 7) to the level i blockade of the 2.0-nm pore using the following equation:

$$\langle \frac{\Delta I}{I_o} \rangle_{MI} = \mathcal{N}^{-1} \left[\phi_M \, e^{\frac{\Delta\Delta G_{MI} + \Delta\Delta H_{MI}^{E_{app}}}{k_B T_0}} + \phi_I \right], \qquad [2]$$

where the fractional blockades for states M and I are given by ϕ_M and ϕ_I, respectively. The normalization is given by $\mathcal{N} = 1 + \exp\{(\Delta\Delta G_{MI} + \Delta\Delta H_{MI}^{E_{app}})/k_B T_0\}$, and T_0 is room temperature. The result of a fit with only the linear E_{app} term in Eq. **1** is given in Table 1 because when both terms are used there are

too many parameters for unique convergence. However, when the opposite limiting case is employed (i.e., using only the quadratic term in E_{app}), the fit results in a polarizability difference $\Delta\alpha_{MI} = 0.4 \pm 0.07$ Debye-m/MV that translates to an induced dipole difference of 46.4 ± 8.2 Debye (when using the midpoint field in Fig. 2*C*, $E_{mid} = 116.6$ MV/m). The similarity between the fits using either the linear- or quadratic-field dependence allows us to use just the linear term as a fitting parameter, so long as we keep in mind that differences between the induced dipoles can also participate in altering the energy gaps between the thermodynamic states. Finally, we note that, at the mouth of the pore, the fractional blockades are much smaller than when the protein transitions to the U state and moves inside the pore, forming the blockade level ii.

To analyze the event durations for each level, we fit the event-duration distribution for each state to exponentially decaying distributions. For level i (Fig. 2*D*), we find a single time constant of $\tau_i = 23.2 \pm 0.9$ ms at −300 mV, which reflects the lifetime at the mouth of the 2.0-nm pore prior to formation of more fully unfolded states that have the potential to thread and generate the higher blockades associated with level ii. As might be expected, there is a monotonic decrease of τ_i beyond −300mV (Fig. 2*F*) reflecting faster conversion to the U-state conformations. In contrast, for the distribution of level ii events, we observe two distinct time constants, a fast timescale τ_{ii1} and a slower timescale, τ_{ii2} (Fig. 2*E*). This indicates that there must be at least two states contributing to level ii that are not easily resolved via their blockade current (although small deviations from the single Gaussian fit in Fig. 2*B* can be discerned). The duration of τ_{ii2} monotonically decreases with increasing voltage beyond −300 mV (Fig. 2*F*), which is consistent with the faster translocation of a threaded state as the voltage is increased. In contrast, the shorter lifetime component ($\tau_{ii1} \sim 0.5$ ms) does not appreciably change at lower voltages, while beyond −500 mV it cannot be resolved from τ_{ii2} (Fig. 2*F*). Possible scenarios for this behavior are discussed in *SI Appendix*, section 21.

Denaturant and Electric-Field–Induced Unfolding during cyt *c* Translocation through a 2.5-nm-Diameter Pore. To experimentally verify electric-field–induced protein unfolding, we investigated the fractional-blockade distributions as a function of voltage for a 2.5-nm-diameter pore for different concentrations of guanidinium hydrochloride (Gdm-Cl), a chaotropic denaturant. Notwithstanding previous studies (60, 61) of cyt *c* at very high (~1 mM) concentrations in 60% ethanol, we observe no evidence of guanidinium-induced aggregation and oligomerization since relatively low fractional blockades are observed, indicating that cyt *c* is in monomeric state at these very low (0.5 to 1.0 μM) concentrations. The plotted distributions (Fig. 3*A*) reveal a clear transition from the native state of the protein to metastable and unfolded states. Below a threshold voltage (<350 mV), we observe exclusively deep blockade ratios (0.8 to 0.9), attributed to interactions of the native state (N) of cyt *c* and conformationally excited states M. In contrast, for voltages above 350 mV, we observe a gradual transition to shallower fractional blockades, indicating further conformational excitation to stretched and unfolded states. We also observed similar behavior in the blockade distributions with respect to voltage for a 3.0-nm pore (*SI Appendix*, section 12 and Fig. S9), where the transition occurred at much lower voltage (V ~−250 mV) as compared to the 2.5-nm pore.

Next, to confirm that our observations can be attributed to protein shape, we performed experiments in the presence of different concentrations of Gdm-Cl (in 1 M KCl, 10 mM Hepes, pH 7.5) using a 2.5-nm pore (*SI Appendix*, section 13, Table S3, and Figs. S10–S15). In the presence of 0.5 M Gdm-Cl (Fig. 3*B*), a transition to unfolded state (low $\Delta I/I_o$) occurs more gradually and begins at lower voltages than in the absence of Gdm-Cl. In contrast, in 2 M Gdm-Cl (Fig. 3*C*), we observe no clear population and no transition, indicating that random portions of the protein are more likely to enter the pore due to its disordered state (data for 1 M Gdm-Cl are presented in *SI Appendix*, Fig. S12). Furthermore, in 3 M Gdm-Cl (*SI Appendix*, section 13 and Figs. S13 and S14), we find a clear peak (around 0.3) in the fractional-blockade distribution, attributed to fully unfolded cyt *c* conformations.

Squeezing and Electric-Field–Induced Unfolding of Distinct Metastable States during cyt *c* Translocation. Next, we examine the detailed process of cyt *c* passage through a 2.5-nm pore as a function of voltage or electric field (E_{app}). In Fig. 3*D*, we plot the mean capture rates as a function of E_{app}. Our finding of a linear increase in capture rate is consistent with drift-limited capture theory (24). Furthermore, this observation, in addition to long measured residence times (relative to our 10 μs measurement time resolution), rules out the possibility of any time resolution artifacts in the entire voltage range of our experiments.

Analysis of the fractional-blockade distributions reveals a total of four distinct populations, and they were fit using a four-component Gaussian where the centroids identify various states of cyt *c* in the pore, as plotted in Fig. 3*E* for each E_{app} (*SI Appendix*, section 14 and Fig. S16). We observe two peaks centered around 0.82 (red markers) and 0.9 (blue markers), which vanish for $E_{app} \gtrsim 200$ MV/m. Between E_{app} ~0 to 30 MV/m, there is a gradual transition from initial native states N to squeezed metastable states, designated as M_1 and M_2, which may differ from each other by how these partially unfolded configurations are able to squeeze into the 2.5-nm pore. As E_{app} is increased into the range ~110 to 170 MV/m, large subsets of the two populations undergo a major dynamic unfolding transition as evidenced by a significant reduction in the fractional blockades (triangles in Fig. 3*E*). These transitions are designated as $M_1 \leftrightarrow U_1$ (blue triangles) and $M_2 \leftrightarrow I \leftrightarrow U_2$ (red triangles). Finally, as E_{app} approaches ~250 MV/m, the protein transitions to a completely unfolded state, which is marked by very low fractional blockades. We envision that the unfolded protein has two types of blockade states (denoted U_1 and U_2) within the pore depending upon the initial squeezing configurations and the ensuing unfolding pathway ($M_1 \leftrightarrow U_1$ or $M_2 \leftrightarrow I \leftrightarrow U_2$).

Energetics of cyt *c* Unfolding. To quantitatively understand the observed electric-field–induced unfolding transition and to evaluate the energy gaps and dipole interactions of the various states, we have considered both a simplified two-state model involving conformational states (M and U), separated by an energy gap $\Delta\Delta G_{MU}$, as well as a sequential three-state unfolding model, which also includes the I state. Both of these models lead to expressions that are analogous to Eq. **2**, and they are discussed more completely in *SI Appendix*, section 15. Because the $M_1 \leftrightarrow U_1$ transition shows a much broader distribution compared to the $M_2 \leftrightarrow I \leftrightarrow U_2$ transition (Fig. 3 *E*, *Inset* and *SI Appendix*, section 14 and Fig. S16), we assume that the $M_1 \leftrightarrow U_1$ distribution of blockade states is related to a more direct transition from M_1 to a

Table 1. Fit parameters from the experimental data ($d_{pore} = 2.0$ nm, $L = 4.1$ nm) in Fig. 2*C* at the mouth of the 2.0 nm pore using Eq. 2 with the linear interaction term ($\Delta p_{MI} E_{app}$)

Parameters	M ↔ I
ϕ_M	0.47 ± 0.04
ϕ_I	0.16 ± 0.02
$\Delta\Delta G_{MI}$	2.4 ± 0.6 kcal/mol
Δp_{MI}	44.0 ± 11.8 Debye

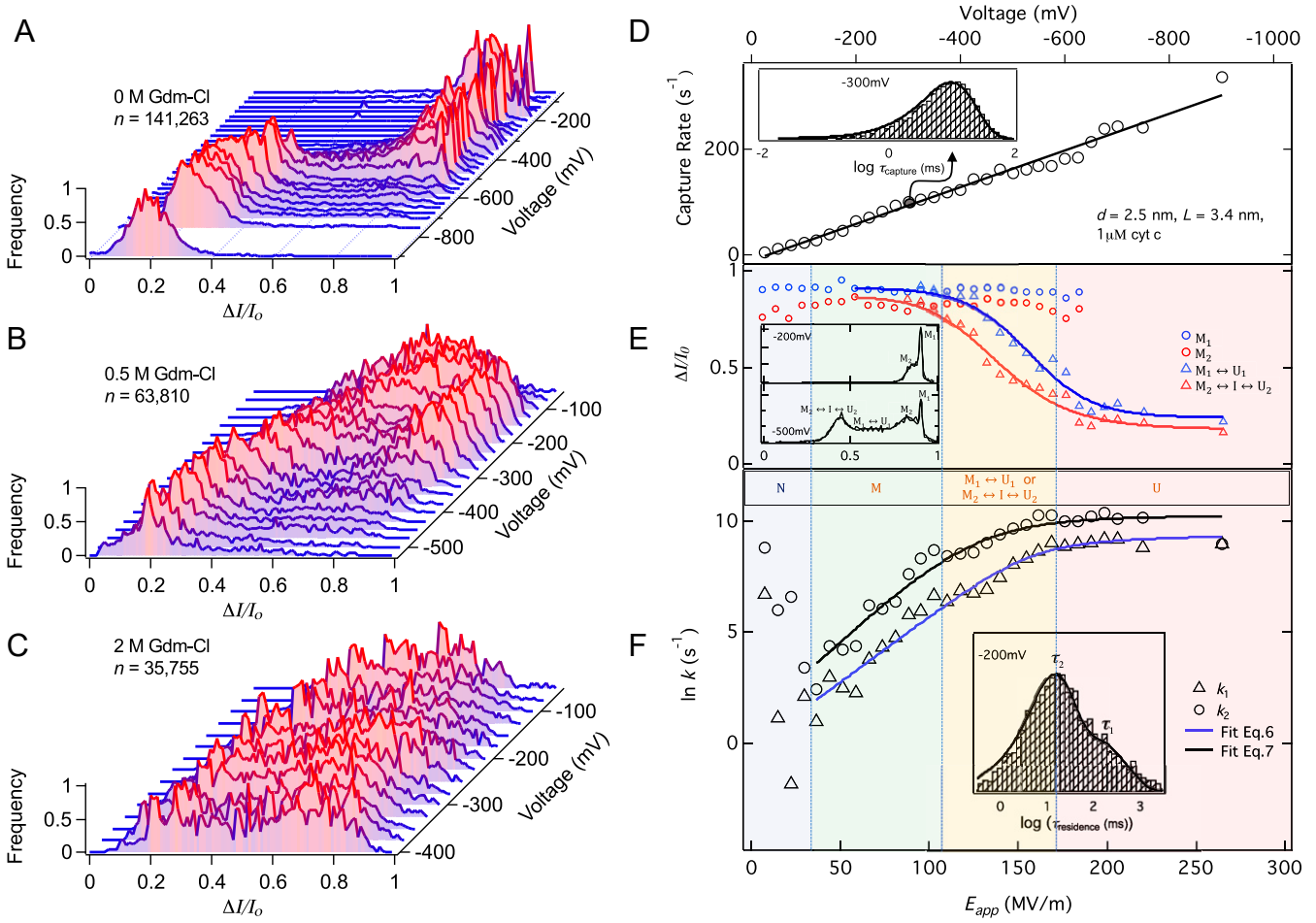

Fig. 3. Electric-field–induced unfolding of cyt *c*: distributions of fractional current blockades as a function of applied voltage measured for pores with d_{pore} = 2.5 nm, L = 3.4 nm. (*A*) In absence of Gdm-Cl ([cyt c] = 1.0 μM), distributions show a clear transition from metastable (higher $\Delta I/I_o$) to unfolded (lower $\Delta I/I_o$) states. (*B*) In presence of 0.5 M Gdm-Cl ([cyt c] = 0.5 μM), distributions show transitions at a lower voltage, and (*C*) in presence of 2 M Gdm-Cl solution ([cyt c] = 0.5 μM), broad distributions without any transition and no well-defined peaks indicate a disordered ensemble of protein conformations. The total number of events collected for each experiment, n, is indicated on each panel. (*D*) Capture rates as a function of applied voltage and electric field, when 1 μM cyt c was placed in the cis compartment. The inset shows a typical distribution of $\log(\tau_{capture})$ measured at −300 mV, and the black solid line represents a single exponential fit to the distribution. (*E*) The mean value of fractional change in current as a function of electric field and applied voltage for different assigned metastable states (M_1, M_2) and dynamically unfolding states ($M_1 \leftrightarrow U_1$, $M_2 \leftrightarrow I \leftrightarrow U_2$). The inset shows typical distributions of fractional change in current, measured at −200 and −500 mV, along with the fits using the multicomponent Gaussian function. The blue curve is fit with the two-state ($M_1 \leftrightarrow U_1$) model, and the red curve is fit with the three-state model ($M_2 \leftrightarrow I \leftrightarrow U_2$). These fits yield the values of $\Delta\Delta G_{MU}$ and Δp_{MU} (see Table 2 and also *SI Appendix*, section 15). (*F*) The rate of protein translocation as a function of applied voltage and electric field. The inset shows a typical distribution of $\tau_{residence}$ measured at −200 mV, and the solid curve represents its fit with a bimodal distribution, yielding two time constants (τ_1 and τ_2) and rates (k_1 and k_2). Reference *SI Appendix*, section 16 and Fig. S17 for $\tau_{residence}$distributions at higher fields. Along with the fractional-blockade distributions shown in *E*, this strongly indicates that there are two distinct metastable state configurations (M_1 and M_2) that can squeeze into the pore. Upon increasing the electric field to ~30 MV/m, the protein is successfully trapped and partially unfolded to form the squeezed M states. As the field increases, transitions take place between the metastable and fully unfolded states ($M_1 \leftrightarrow U_1$ and $M_2 \leftrightarrow I \leftrightarrow U_2$). The higher field leads to a higher probability of U-state formation and much faster translocation. Saturation of fully unfolded protein occurs above ~200 MV/m.

random set of unfolded conformations U_1, which translocate at differing rates centered around the mean value. This suggests a direct, nonsequential, unfolding pathway between M_1 and U_1 exists within the pore. For the $M_2 \leftrightarrow I \leftrightarrow U_2$ transition, we assume a sequential pathway where one of the α-helices unfolds first, forming the I state, followed by the other two α-helices to form the U state (32, 58). Thus, the blue triangles, which are a measure of the mean of the $M_1 \leftrightarrow U_1$ blockade distribution, are fit using a simple two-state $M_1 \leftrightarrow U_1$ model (*SI Appendix*, section 15 and Eq. **S8**), which yields $\Delta\Delta G_{M_1U_1} = 5.3$kcal/mol (Table 2). On the other hand, the mean of the blockade distribution for $M_2 \leftrightarrow I \leftrightarrow U_2$ (red triangles Fig. 3*E*) is described using the three-state sequential unfolding model (*SI Appendix*, section 15 and Eq. **S7**), which is constrained by the $M \leftrightarrow I$ parameter values found previously (Table 1). This approach yields a similar transition energy between M and U (i.e., $\Delta\Delta G_{M_2U_2} = 5.4$ kcal/mol, Table 2).

Thus, both the $M_1 \leftrightarrow U_1$ and $M_2 \leftrightarrow U_2$ free energy gaps are found to be in excellent agreement with the value of the total free energy, 5.4 kcal/mol, previously found (32) for unfolding the three major α-helical regions of cyt *c*. It is also worthwhile to mention that a threshold voltage required to rupture a protein–DNA complex using a solid-state nanopore was previously found to correlate well with the equilibrium free energy of the complex formation (62). Finally, we note that the initial breakage of the salt bridge, involving E62, and the partial unfolding that leads to formation of the squeezed M state,

Table 2. Fit parameters from the experimental data (d_{pore} = 2.5 nm, L = 3.4 nm) in Fig. 3*E* using two-state and three-state models (*SI Appendix*, section 15 and Eqs. S8 and S7, respectively)

Parameters	$M_1 \leftrightarrow U_1$	$M_2 \leftrightarrow I \leftrightarrow U_2$
ϕ_M	0.91 ± 0.02	0.86 ± 0.02
ϕ_I	—	0.86 ± 0.02
ϕ_U	0.24 ± 0.02	0.18 ± 0.03
$\Delta\Delta G_{MI}$ (Table 1)	—	2.4 kcal/mol
$\Delta\Delta G_{MU}$	5.3 ± 0.5 kcal/mol	5.4 ± 0.6 kcal/mol
Δp_{MI} (Table 1)	—	44 Debye
Δp_{MU}	70.2 ± 7.4 Debye	91.4 ± 8.5 Debye

should leave the free energy gap between M and U unaffected. This is verified by independent studies using an E62G mutation to remove the salt bridge, which demonstrated that the $\Delta\Delta G_{MU}$ energy gap remains unchanged (32, 58).

Kinetics of cyt *c* Translocation. In order to discern the kinetics of translocation of metastable and unfolded states, we analyzed the rate $k_{tr} = 1/\langle\tau_{residence}\rangle$ of protein translocation as a function of voltage and electric field (for $E_{app} \gtrsim 30$ MV/m) where we again make use of the fast α-helical folding/unfolding transitions (51–56) relative to the experimental (~ms) translocation times. Thus, the thermodynamically averaged translocation rates for the two- and three-state models can be expressed as follows:

$$k_{tr} = P_M k_M + P_U k_U \ (M \leftrightarrow U) \quad [3]$$

or

$$k_{tr} = P_M k_M + P_I k_I + P_U k_U \ (M \leftrightarrow I \leftrightarrow U), \quad [4]$$

where P_J is the E_{app} dependent probability of finding cyt c in the J^{th}state, and k_J is the E_{app} dependent translocation rate of the J^{th} state (J = M, I, U).

For the U and I states, we assume the field-dependent translocation rates are given by the following:

$$k_U = k_{0U}\, e^{\frac{\beta_U E_{app}}{k_B T_0}}, \text{ and } k_I = k_{0I}\, e^{\frac{\beta_I E_{app}}{k_B T_0}}, \quad [5]$$

with $k_{0J} = k_a\, e^{-\frac{\Delta G_J^{tr}}{k_B T_0}}$. The Arrhenius prefactor, k_a, is estimated below and, for simplicity, we assume that $k_M \cong 0$ for the 2.5-nm pore. The unknown parameters, β_U and β_I, account for the translocation barrier reduction due to the electrophoretic forces. This parameter can be combined with the state-dependent dipole difference values (Eq. **1**), associated with P_J, and obtained from the fits to the blockade ratio analysis (Table 2). Thus, upon combining, we can define $\beta_I^* = \beta_I + \Delta p_{MI}$ and $\beta_U^* = \beta_U + \Delta p_{MU}$, which become the final fitting parameters for analysis of the translocation rates. When the zero-field free energy gaps are constrained by the values found in Table 2, the expression for the translocation rate in the two-state model (with $k_M \cong 0$) depends only on k_{0U} and $\beta_U = \beta_U^* - \Delta p_{MU}$ (reference *SI Appendix*, section 17):

$$k_{tr(M \leftrightarrow U)} = \mathcal{N}^{-1}\left[k_{0U}\, e^{-\frac{\{\Delta\Delta G_{MU} - \beta_U^* E_{app}\}}{k_B T_0}}\right], \quad [6]$$

with

$$\mathcal{N} = \left[1 + e^{-\frac{\{\Delta\Delta G_{MU} - \Delta p_{MU} E_{app}\}}{k_B T_0}}\right].$$

For the three-state model, we use the following equation:

$$k_{tr(M \leftrightarrow I \leftrightarrow U)} = \mathcal{N}^{-1}\left[k_{0U} e^{-\frac{\{\Delta\Delta G_{MU} - \beta_U^* E_{app}\}}{k_B T_0}} + k_{0I}\, e^{-\frac{\{\Delta\Delta G_{MI} - \beta_I^* E_{app}\}}{k_B T_0}}\right], \quad [7]$$

with

$$\mathcal{N} = \left[1 + e^{-\frac{\{\Delta\Delta G_{MI} - \Delta p_{MI} E_{app}\}}{k_B T_0}} + e^{-\frac{\{\Delta\Delta G_{MU} - \Delta p_{MU} E_{app}\}}{k_B T_0}}\right].$$

As shown in the plot of ln $[k_{tr}]$ (Fig. 3*F*), after trapping and conversion to the squeezed M state, there is an increase in translocation rate as a function of the electric field above ~30 MV/m. Additionally, at each voltage, we observed two distinct rate distributions (Fig. 3 *F*, *Inset* and *SI Appendix*, section 16 and Fig. S17), which we attribute to the translocation of two distinct conformationally excited states as noted in the caption of Fig. 3*F*.

Below 30 MV/m, $1/\langle\tau_{residence}\rangle$ decreases with voltage, and we attribute this behavior to the increased time spent by the N state of cyt c as it is trapped at the pore mouth. At these low electric fields, the energy of the excited states on the unfolding pathway of cyt c are not lowered sufficiently to allow thermal excitation from N to M. However, in the regime between 30 to 100 MV/m, ln $[k_{tr}]$ starts to increase with the electric field, manifesting the conformational excitation to the M state and its rapid thermodynamic exchange with the I and U states, which also have reduced free energy gaps due to the electric field interaction. Consistent with the blockade ratio results presented above, we assigned two distinct rates in this regime to the two metastable states, M_1 and M_2, differing by a small amount, presumably due to different trapping configurations of the M state within the pore. Between 100 to 170 MV/m, the increase of ln $[k_{tr}]$ begins to diminish, while above 170 MV/m the rate levels off. This is attributable to the saturation of the U-state population (and its associated distribution of blockade ratios and translocation times) as the electric field is increased.

The fitting parameters for the solid dark lines in Fig. 3*F*, found using Eqs. **6** and **7**, are listed in Table 3. It can be seen that the U state has the dominant rate for translocation compared to the I state (and the M-state rate was assumed to be small enough that it was neglected in the field-dependent kinetic analysis). Moreover, β_U, which governs the field dependence of the U-state translocation rate, is seen to be negligible compared to the dipole difference, suggesting that the electrophoretic work done by the field, which lowers the U-state translocation barrier, is relatively small for the 2.5-nm pore. However, it should be noted that $\beta_I = 47$ Debye is much larger than $\beta_U = 2 - 3$ Debye, suggesting there is much more resistance to the electrophoretic forces acting to pull the I-state protein through the 2.5-nm pore.

Table 3. Parameters from the fit of kinetic data (Fig. 3*F*) using Eq. 6 for k_1 (triangles) and Eq. 7 for k_2 (circles)

Parameters (Eq. **6**)	$M_1 \leftrightarrow U_1$
k_{0U}	5,839 ± 1,260 s^{-1}
β_U	3.0 ± 1.8 Debye
Δp_{MU} (Table 2)	70.2 Debye
$\Delta\Delta G_{MU}$ (Table 2)	5.3 kcal/mol
Parameters (Eq. **7**)	$M_2 \leftrightarrow I \leftrightarrow U_2$
k_{0U}	10,712 ± 1,290 s^{-1}
β_U	1.75 ± 1.04 Debye
Δp_{MU} (Table 2)	91.4 Debye
k_{0I}	72 ± 13 s^{-1}
β_I	47.2 ± 7 Debye
Δp_{MI} (Table 2)	44 Debye
$\Delta\Delta G_{MU}$ (Table 2)	5.4 kcal/mol
$\Delta\Delta G_{MI}$ (Table 2)	2.4 kcal/mol

This is also evidenced by its much slower zero-field rate, $k_{0I} = 72\ s^{-1}$, compared to $k_{0U} = 10712\ s^{-1}$. Additional analysis of the 2.0-nm pore data (e.g., Fig. 2*E*) in *SI Appendix*, section 18 and Fig. S19 yields a low field slope indicating that β_U for the 2.0-nm pore is about an order of magnitude larger than found for the 2.5-nm pore, while the intercept at zero field suggests $k_{0U} \sim 5s^{-1}$ for the 2.0-nm pore.

As can be seen in Table 3, there is a dominant k_{0U} translocation rate extracted for the two U-state configurations. These separate rates derive from the different configurations of their parent states, M_1 and M_2. To evaluate the translocation barriers for $\Delta G^{\ddagger tr}_{U_1}$ and $\Delta G^{\ddagger tr}_{U_2}$, we can use a simple Arrhenius equation for the rate in zero field:

$$\ln k_{0U} = \ln k_a - \frac{\Delta G^{\ddagger tr}_{U}}{k_B T_0}, \qquad [8]$$

where k_a is the rate of translocation at zero electric field without any activation barrier (i.e., no pore). This can be calculated from the rate at which cyt *c* moves a distance comparable to the length (L) of the pore. Thus, assuming Stokes–Einstein diffusion of cyt *c* in bulk solution, $k_a = \frac{k_B T_0}{6\pi\,\eta\,R_{cyt\,c}\,L^2}$, where η is the viscosity of water (1 centipoise) and $R_{cyt\,c}$ is the hydrodynamic radius of cyt *c* (~1.5 nm). Using these values and L = 3.4 nm, we find $k_a = 1.26 \times 10^7 s^{-1}$. The values for k_{0U} in Table 3 for the 2.5-nm pore, along with Eq. **8**, then lead to the following: $\Delta G^{\ddagger tr}_{U_1} \cong 7.7\,k_B T_0$ and $\Delta G^{\ddagger tr}_{U_2} \cong 7.1\ k_B T_0$. Using the I-state rate, $k_{0I} = 72\ s^{-1}$, we can similarly deduce that $\Delta G^{\ddagger tr}_{I} \cong 12\ k_B T_0$. Finally, if we extrapolate the triangle data points in Fig. 3*F* to zero electric field and attribute this to M_1 translocation, we can estimate a zero-field rate $k_{0M_1} \sim 0.8\ s^{-1}$. Similarly, by extrapolating the circle data points in Fig. 3*F* to zero field, we can estimate $k_{0M_2} \sim 1.3\ s^{-1}$. Thus, by using Eq. **8**, we can deduce $\Delta G^{\ddagger tr}_{M_1} \sim 17\ k_B T_0$ and $\Delta G^{\ddagger tr}_{M_2} \sim 16\ k_B T_0$.

MD Simulations. To confirm that electric field alone can indeed produce unidirectional translocation of cyt *c* protein through a solid-state nanopore and to relate protein unfolding to nanopore diameter and changes in the ionic current blockade levels, we performed all-atom MD simulations of six nanopore systems, varying in diameter from 5.5 to 1.5 nm (Fig. 4*A* and *SI Appendix*, section 11, Table S2, and Figs. S7 and S8). Each simulation system contained one Si_3N_4 nanopore, one cyt *c* protein placed in front of the nanopore, and 1 M KCl solution. Following equilibration, each system was simulated using the grid-steered molecular dynamics (G-SMD) protocol (63), where the open-pore electrostatic potential map, amplified by a scaling factor, was used to drive the translocation of the cyt *c* protein with an accelerated rate. To eliminate the uncertainty associated with various paths the protein could take to enter the nanopore, the protein was additionally restrained to have its center of mass located along the pore axis. The simulations were carried out at effective biases of 1, 2, and 3 V, which allowed us to observe complete permeation events for the majority of the nanopore systems within a 100 ns time scale, Fig. 4*B*. Such a dramatic acceleration of the translocation process is expected as the rate of a forced barrier crossing exponentially depends on the magnitude of the applied force (64). Fig. 4 *B*–*G* summarize the simulation results.

We found the pore diameter to have a pronounced effect on the time scale and the character of cyt *c* translocation. When the pore was slightly larger (d = 5.5 nm) than the protein, the translocation proceeded very fast (<1 ns, Fig. 4*B*) and produced well-defined shallow blockades of the nanopore current, see Fig. 4*C*. The protein structure, which we characterize here as the fraction of native contacts remaining, that is, the Q value (65), remained largely unperturbed by the nanopore passage, see Fig. 4*D*. The translocation through a nanopore that was slightly smaller (d = 3.5 nm) than the protein proceeded via reversible squeezing of the protein that largely preserved the secondary structure. The protein was found to block nearly 90% of the ionic current when confined to the pore constriction. A qualitatively different behavior was observed for 3.0-, 2.5-, and 2.0-nm-diameter pore: the protein was found to partially unfold during the translocation, with the average degree of unfolding, see Fig. 4*E*, decreasing with larger pore diameters. The average translocation time was found to exponentially depend on the pore diameter, see Fig. 4*F*, whereas the maximum current blockade ratio [computed using SEM approach (66)] during the translocation, see Fig. 4*G*, reached nearly 100% of the open-pore current. Interestingly, in our simulations, we did not observe cyt *c* passage through the 1.5-nm-diameter nanopore, unless the protein was mechanically unfolded by the application of external force to a protein terminus (*SI Appendix*, section 11 and Fig. S8).

Discussion

One striking feature of our analysis is that for a 2.5-nm pore, the values of $\Delta G^{\ddagger tr}_{M_1}$ and $\Delta G^{\ddagger tr}_{M_2}$ (estimated by use of Eq. **8** and straight line extrapolation of the rates to zero electric field as in *SI Appendix*, section 19 and Table S7) are less than that of the unfolding barrier ($\Delta G^{\ddagger}_{NU} > 21.6 k_B T_0$, with $k_B T_0 = 0.59$ kcal/mol) reported in an earlier study (32). Thus, squeezing of cyt *c* via metastable conformations M_1 and M_2 into the pore is an energetically favorable path compared to the requirement that the protein completely unfolds and translocates via threading. The value of $\Delta G^{\ddagger tr}_{M}$ is also clearly greater than $\Delta G^{\ddagger}_{NU}$ in the experiments with the 1.5- and 2.0-nm pores (*SI Appendix*, section 18 and Fig. S19). Thus, for the smaller pores, excitation from M to a higher energy conformational state, I, at the pore mouth, followed by unfolding-mediated threading of the U state is the favorable path for translocation.

Another remarkable point is that the values of $\Delta\Delta G_{MI} = 2.4$ kcal/mol (Table 1), $\Delta\Delta G_{M_1U_1} = 5.3$ kcal/mol, and $\Delta\Delta G_{M_2U_2} = 5.4$ kcal/mol (Table 2) obtained from the analysis are in very close agreement with the cyt *c* α-helix unfolding transitions reported in previous work (32, 58). In the prior studies, a 2.6 kcal/mol free energy gap was found between a partially unfolded state ~ 7.4 kcal/mol above the N-state (which we identify as the M state with the three main α-helices still folded) and the next higher state on the unfolding pathway (which we identify as the I state) where the α-helix associated with residues 61 to 68 has unfolded. Moreover, the free energy gap from M to the fully unfolded state U was found in prior work (32) to be 5.4 kcal/mol, almost exactly the value found for both of the configurations (M_1 and M_2) within the pore.

In summary, we have demonstrated protein translocation through a pore barrier ($d_{pore} < d_{protein}$) without any requirement of chemical denaturants, an enzymatic motor, or an oligo tag. We achieved this by electric-field manipulation of the conformational energy levels of a protein in the vicinity of the pore. We find that cyt *c* is able to squeeze into the 2.5-nm pore where it can still undergo rapid conformational transitions between folded and unfolded α-helical states. The protein then translocates through the pore with a rate that depends upon the thermodynamic probability to completely unfold the residual α-helices. In contrast, for 2.0- and 1.5-nm pores, cyt *c* undergoes conformational excitations at the mouth of the pore first from state M, with all three α-helices intact (32, 58, 59), to state I, with only a residual bihelical segment (32, 58, 59), and finally to the fully unfolded state so that entry and translocation occurs only via threading through the pore. These results demonstrate that the necessity of complete unfolding for a protein to enter and translocate depends upon the diameter of the pore. The relatively large field strengths (~10^7 to 10^8 V/m), needed for translocation in these experiments, owe to the more rigid nature

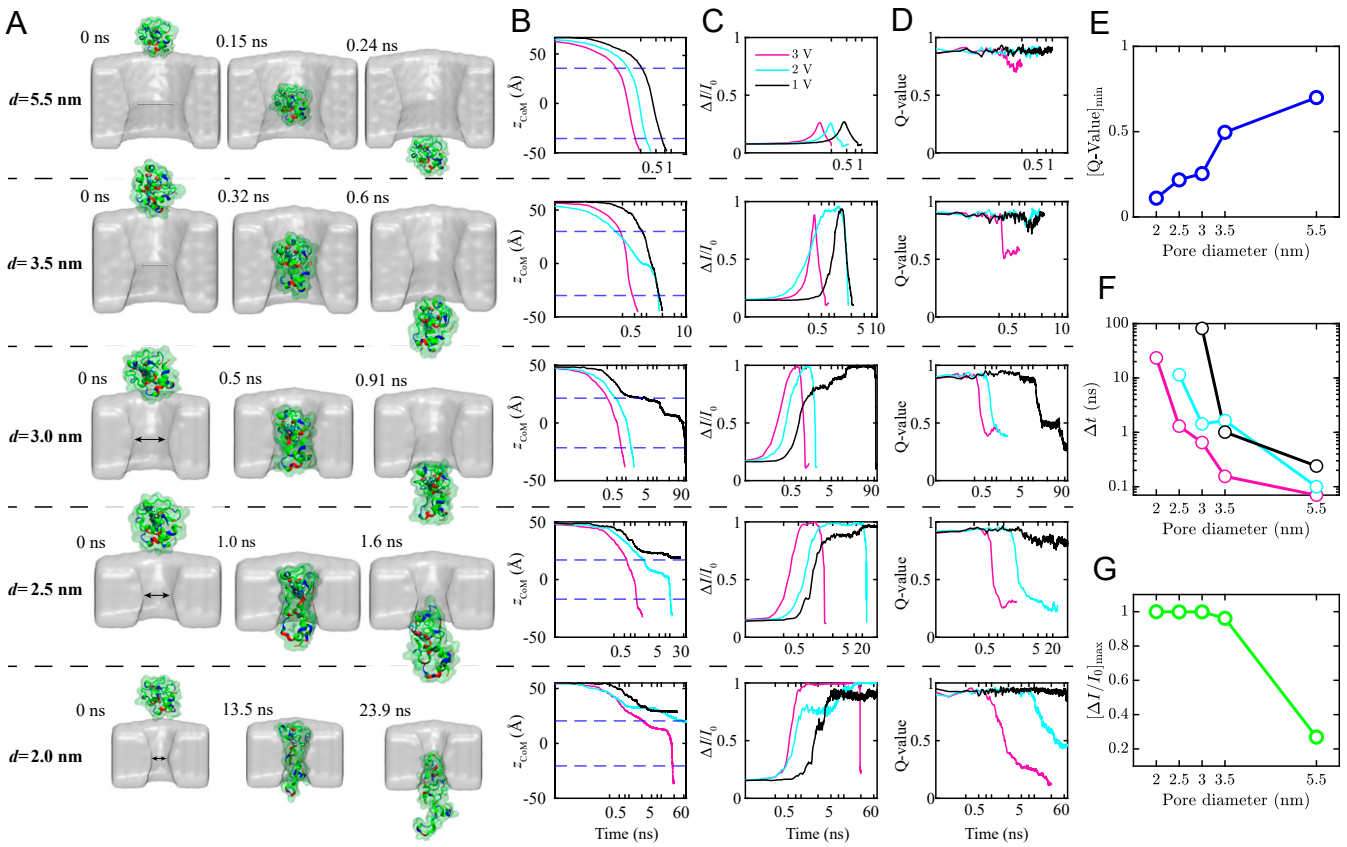

Fig. 4. MD simulations of cyt *c* passage through nanopores. (*A*) Snapshots illustrating five MD trajectories where a single cyt *c* protein (shown as a cartoon enclosed by a semitransparent surface) was forced to pass through a nanopore (gray) of specified diameter *d* using the G-SMD protocol (*SI Appendix*, section 11, *iii*) under a 3 V effective bias. (*B–D*) Center of mass z coordinate (*B*), ionic current blockade (*C*), and the fraction of native protein contacts, Q-value (*D*), versus simulation time for three G-SMD simulations carried out at the effective biases of 1 (black), 2 (cyan), and 3 (pink) V. The pore diameter *d* was, from top to bottom, 5.5, 3.5, 3.0, 2.5, and 2.0 nm. The ionic currents were computed using the SEM approach (*SI Appendix*, section 11, *iv*). Note the logarithmic scale of the time axis. (*E–G*) Minimum Q-value (*E*), nanopore translocation time (*F*, logarithmic scale), and maximum blockade current amplitude (*G*) observed during the MD simulations as a function of the pore diameter.

of the SiN pore as compared to biological membrane pores, where typical electric-field values that are used in translocation measurements are lower ($\lesssim 10^7$ V/m i.e., $\lesssim$50 mV/5 nm).

The experiments reported here set the stage for new studies where electrical manipulations sculpt the conformational landscape of proteins. Detection of protein signatures and folding patterns as they pass in unique ways through a nanopore can also serve as the basis of their identification, and this approach requires only a localized electric field without any additional requirements such as enzymes, oligo tags, or chemical denaturants. Future studies will examine the behavior of other proteins using similar experiments and comparisons among protein structural variants and proteins with and without posttranslational modifications.

Materials and Methods

We assembled the solid-state nanopore chips in a flow cell that separates two compartments, cis and trans, each containing 1 M KCl and 10 mM Hepes (pH 7.5) buffer solution (see Fig. 1*A*). To observe cyt *c* interactions with a pore, we placed 0.5 or 1.0 μM of cyt *c* (1 μM in absence of Gdm-Cl and 0.5 μM M in presence of Gdm-Cl) in the cis compartment and applied a negative potential (−25 to −900 mV) to the trans compartment while keeping cis grounded. This generates a strong pore-localized electric field (~10^8 V/m) oriented in the cis to trans direction, which results in ion current that is subject to modulation when cyt *c* is trapped or enters the pore.

We used previously reported wafer-fabrication methods (30, 50, 67, 68) to drill ultrathin solid-state nanopores in the diameter range of 1.5 to 5.5 nm in high-stress negatively charged SiN membranes (*SI Appendix*, section 3 and Fig. S2). Based on the measured conductance across the pores (*SI Appendix*, section 4 and Table S1), we used a standard procedure (67–69) to obtain the effective pore length *L*, as indicated in the figure captions. Additional chemical materials and experimental methods are described in *SI Appendix*, sections 1 and 2, and MD simulation methods are described in *SI Appendix*, section 11.

Data Availability. Datasets used to make figures have been deposited in Figshare (https://figshare.com/s/1e72a37e71f1a8ae4090).

ACKNOWLEDGMENTS. P.T. thanks Mehrnaz Mojtabavi for assistance with the gel electrophoresis experiments and for providing access to the laboratory computer during the COVID-19 outbreak. This work was supported by the NSF through grants DMR-1710211 (M.W.), DMR-1827346 (A.A.), and CHE-1764221 (P.M.C.). Computer time was provided through Extreme Science and Engineering Discovery Environment allocation MCA05S028.

1. B. Alberts, *Molecular Biology of the Cell* (Garland Science, New York, 2008).
2. W. Wickner, R. Schekman, Protein translocation across biological membranes. *Science* **310**, 1452–1456 (2005).
3. S. Huang, K. S. Ratliff, A. Matouschek, Protein unfolding by the mitochondrial membrane potential. *Nat. Struct. Biol.* **9**, 301–307 (2002).
4. R. J. Collier, Membrane translocation by anthrax toxin. *Mol. Aspects Med.* **30**, 413–422 (2009).
5. A. Martin, T. A. Baker, R. T. Sauer, Pore loops of the AAA+ ClpX machine grip substrates to drive translocation and unfolding. *Nat. Struct. Mol. Biol.* **15**, 1147–1151 (2008).
6. S. Orrenius, B. Zhivotovsky, Cardiolipin oxidation sets cytochrome c free. *Nat. Chem. Biol.* **1**, 188–189 (2005).
7. G. Oukhaled *et al.*, Unfolding of proteins and long transient conformations detected by single nanopore recording. *Phys. Rev. Lett.* **98**, 158101 (2007).
8. B. Cressiot *et al.*, Protein transport through a narrow solid-state nanopore at high voltage: Experiments and theory. *ACS Nano* **6**, 6236–6243 (2012).
9. A. Oukhaled *et al.*, Dynamics of completely unfolded and native proteins through solid-state nanopores as a function of electric driving force. *ACS Nano* **5**, 3628–3638 (2011).

10. M. Pastoriza-Gallego *et al.*, Dynamics of unfolded protein transport through an aerolysin pore. *J. Am. Chem. Soc.* **133**, 2923–2931 (2011).
11. J. Nivala, D. B. Marks, M. Akeson, Unfoldase-mediated protein translocation through an α-hemolysin nanopore. *Nat. Biotechnol.* **31**, 247–250 (2013).
12. D. Rodriguez-Larrea, H. Bayley, Multistep protein unfolding during nanopore translocation. *Nat. Nanotechnol.* **8**, 288–295 (2013).
13. D. Rodriguez-Larrea, H. Bayley, Protein co-translocational unfolding depends on the direction of pulling. *Nat. Commun.* **5**, 4841 (2014).
14. D. S. Talaga, J. Li, Single-molecule protein unfolding in solid state nanopores. *J. Am. Chem. Soc.* **131**, 9287–9297 (2009).
15. D. J. Niedzwiecki, J. Grazul, L. Movileanu, Single-molecule observation of protein adsorption onto an inorganic surface. *J. Am. Chem. Soc.* **132**, 10816–10822 (2010).
16. J. Houghtaling *et al.*, Estimation of shape, volume, and dipole moment of individual proteins freely transiting a synthetic nanopore. *ACS Nano* **13**, 5231–5242 (2019).
17. C. Plesa *et al.*, Fast translocation of proteins through solid state nanopores. *Nano Lett.* **13**, 658–663 (2013).
18. E. C. Yusko *et al.*, Controlling protein translocation through nanopores with bio-inspired fluid walls. *Nat. Nanotechnol.* **6**, 253–260 (2011).
19. K. J. Freedman, S. R. Haq, J. B. Edel, P. Jemth, M. J. Kim, Single molecule unfolding and stretching of protein domains inside a solid-state nanopore by electric field. *Sci. Rep.* **3**, 1638 (2013).
20. J. Larkin, R. Y. Henley, M. Muthukumar, J. K. Rosenstein, M. Wanunu, High-bandwidth protein analysis using solid-state nanopores. *Biophys. J.* **106**, 696–704 (2014).
21. P. Waduge *et al.*, Nanopore-based measurements of protein size, fluctuations, and conformational changes. *ACS Nano* **11**, 5706–5716 (2017).
22. R. Hu *et al.*, Differential enzyme flexibility probed using solid-state nanopores. *ACS Nano* **12**, 4494–4502 (2018).
23. L. Movileanu, Squeezing a single polypeptide through a nanopore. *Soft Matter* **4**, 925–931 (2008).
24. M. Muthukumar, *Polymer Translocation* (CRC PRESS, Boca Raton, FL, 2019).
25. I. Nir, D. Huttner, A. Meller, Direct sensing and discrimination among ubiquitin and ubiquitin chains using solid-state nanopores. *Biophys. J.* **108**, 2340–2349 (2015).
26. O. K. Dudko, J. Mathé, A. Szabo, A. Meller, G. Hummer, Extracting kinetics from single-molecule force spectroscopy: Nanopore unzipping of DNA hairpins. *Biophys. J.* **92**, 4188–4195 (2007).
27. J. Mathé, H. Visram, V. Viasnoff, Y. Rabin, A. Meller, Nanopore unzipping of individual DNA hairpin molecules. *Biophys. J.* **87**, 3205–3212 (2004).
28. J. Mathé, A. Aksimentiev, D. R. Nelson, K. Schulten, A. Meller, Orientation discrimination of single-stranded DNA inside the alpha-hemolysin membrane channel. *Proc. Natl. Acad. Sci. U.S.A.* **102**, 12377–12382 (2005).
29. J. B. Heng *et al.*, Stretching DNA using the electric field in a synthetic nanopore. *Nano Lett.* **5**, 1883–1888 (2005).
30. S. Carson, J. Wilson, A. Aksimentiev, M. Wanunu, Smooth DNA transport through a narrowed pore geometry. *Biophys. J.* **107**, 2381–2393 (2014).
31. Y. Bai, T. R. Sosnick, L. Mayne, S. W. Englander, Protein folding intermediates: Native-state hydrogen exchange. *Science* **269**, 192–197 (1995).
32. W. Hu, Z. Y. Kan, L. Mayne, S. W. Englander, Cytochrome c folds through foldon-dependent native-like intermediates in an ordered pathway. *Proc. Natl. Acad. Sci. U.S.A.* **113**, 3809–3814 (2016).
33. H. Roder, G. A. Elöve, S. W. Englander, Structural characterization of folding intermediates in cytochrome c by H-exchange labelling and proton NMR. *Nature* **335**, 700–704 (1988).
34. P. M. De Biase *et al.*, Molecular basis for the electric field modulation of cytochrome C structure and function. *J. Am. Chem. Soc.* **131**, 16248–16256 (2009).
35. M. Saito, S. J. Korsmeyer, P. H. Schlesinger, BAX-dependent transport of cytochrome c reconstituted in pure liposomes. *Nat. Cell Biol.* **2**, 553–555 (2000).
36. S. Shimizu, M. Narita, Y. Tsujimoto, Bcl-2 family proteins regulate the release of apoptogenic cytochrome c by the mitochondrial channel VDAC. *Nature* **399**, 483–487 (1999).
37. Y. Chen *et al.*, How can proteins enter the interior of a MOF? Investigation of cytochrome c translocation into a MOF consisting of mesoporous cages with microporous windows. *J. Am. Chem. Soc.* **134**, 13188–13191 (2012).
38. G. Taler, A. Schejter, G. Navon, I. Vig, E. Margoliash, The nature of the thermal equilibrium affecting the iron coordination of ferric cytochrome c. *Biochemistry* **34**, 14209–14212 (1995).
39. G. A. Elöve, A. K. Bhuyan, H. Roder, Kinetic mechanism of cytochrome c folding: Involvement of the heme and its ligands. *Biochemistry* **33**, 6925–6935 (1994).
40. S. Berezhna, H. Wohlrab, P. M. Champion, Resonance Raman investigations of cytochrome c conformational change upon interaction with the membranes of intact and Ca2+-exposed mitochondria. *Biochemistry* **42**, 6149–6158 (2003).
41. Y. Sun, V. Karunakaran, P. M. Champion, Investigations of the low-frequency spectral density of cytochrome c upon equilibrium unfolding. *J. Phys. Chem. B* **117**, 9615–9625 (2013).
42. A. Benabbas, P. M. Champion, Adiabatic ligand binding in heme proteins: Ultrafast kinetics of methionine rebinding in ferrous cytochrome c. *J. Phys. Chem. B* **122**, 11431–11439 (2018).
43. L. C. Godoy *et al.*, Disruption of the M80-Fe ligation stimulates the translocation of cytochrome c to the cytoplasm and nucleus in nonapoptotic cells. *Proc. Natl. Acad. Sci. U.S.A.* **106**, 2653–2658 (2009).
44. J. Hanske *et al.*, Conformational properties of cardiolipin-bound cytochrome c. *Proc. Natl. Acad. Sci. U.S.A.* **109**, 125–130 (2012).
45. J. P. Kitt, D. A. Bryce, S. D. Minteer, J. M. Harris, Raman spectroscopy reveals selective interactions of cytochrome c with cardiolipin that correlate with membrane permeability. *J. Am. Chem. Soc.* **139**, 3851–3860 (2017).
46. L. J. McClelland, T. C. Mou, M. E. Jeakins-Cooley, S. R. Sprang, B. E. Bowler, Structure of a mitochondrial cytochrome c conformer competent for peroxidase activity. *Proc. Natl. Acad. Sci. U.S.A.* **111**, 6648–6653 (2014).
47. X. Kang, M. A. Alibakhshi, M. Wanunu, One-pot species release and nanopore detection in a voltage-stable lipid bilayer platform. *Nano Lett.* **19**, 9145–9153 (2019).
48. C. Dekker, Solid-state nanopores. *Nat. Nanotechnol.* **2**, 209–215 (2007).
49. M. Wanunu, Nanopores: A journey towards DNA sequencing. *Phys. Life Rev.* **9**, 125–158 (2012).
50. M. Wanunu, W. Morrison, Y. Rabin, A. Y. Grosberg, A. Meller, Electrostatic focusing of unlabelled DNA into nanoscale pores using a salt gradient. *Nat. Nanotechnol.* **5**, 160–165 (2010).
51. J. A. Ihalainen *et al.*, α-Helix folding in the presence of structural constraints. *Proc. Natl. Acad. Sci. U.S.A.* **105**, 9588–9593 (2008).
52. J. H. Werner, R. B. Dyer, R. M. Fesinmeyer, N. H. Andersen, Dynamics of the primary processes of protein folding: Helix nucleation. *J. Phys. Chem. B* **106**, 487–494 (2002).
53. E. A. Gooding *et al.*, The effects of individual amino acids on the fast folding dynamics of α-helical peptides. *Chem. Commun. (Camb.)* 5985–5987 (2005).
54. K. Kuczera, G. S. Jas, R. Elber, Kinetics of helix unfolding: Molecular dynamics simulations with milestoning. *J. Phys. Chem. A* **113**, 7461–7473 (2009).
55. G. S. Jas, K. Kuczera, Helix-coil transition courses through multiple pathways and intermediates: Fast kinetic measurements and dimensionality reduction. *J. Phys. Chem. B* **122**, 10806–10816 (2018).
56. C. S. H. Jesus, P. F. Cruz, L. G. Arnaut, R. M. M. Brito, C. Serpa, One peptide reveals the two faces of α-helix unfolding-folding dynamics. *J. Phys. Chem. B* **122**, 3790–3800 (2018).
57. W. Si, A. Aksimentiev, Nanopore sensing of protein folding. *ACS Nano* **11**, 7091–7100 (2017).
58. H. Maity, M. Maity, S. W. Englander, How cytochrome c folds, and why: Submolecular foldon units and their stepwise sequential stabilization. *J. Mol. Biol.* **343**, 223–233 (2004).
59. M. M. Krishna, Y. Lin, J. N. Rumbley, S. W. Englander, Cooperative omega loops in cytochrome c: Role in folding and function. *J. Mol. Biol.* **331**, 29–36 (2003).
60. P. P. Parui *et al.*, Formation of oligomeric cytochrome c during folding by intermolecular hydrophobic interaction between N- and C-terminal α-helices. *Biochemistry* **52**, 8732–8744 (2013).
61. S. Hirota *et al.*, Cytochrome c polymerization by successive domain swapping at the C-terminal helix. *Proc. Natl. Acad. Sci. U.S.A.* **107**, 12854–12859 (2010).
62. B. Dorvel *et al.*, Analyzing the forces binding a restriction endonuclease to DNA using a synthetic nanopore. *Nucleic Acids Res.* **37**, 4170–4179 (2009).
63. D. B. Wells, V. Abramkina, A. Aksimentiev, Exploring transmembrane transport through α-hemolysin with grid-steered molecular dynamics. *J. Chem. Phys.* **127**, 125101 (2007).
64. E. Evans, Probing the relation between force–lifetime–and chemistry in single molecular bonds. *Annu. Rev. Biophys. Biomol. Struct.* **30**, 105–128 (2001).
65. M. P. Eastwood, C. Hardin, Z. Luthey-Schulten, P. G. Wolynes, Evaluating protein structure-prediction schemes using energy landscape theory. *IBM J. Res. Develop.* **45**, 475–497 (2001).
66. J. Wilson, K. Sarthak, W. Si, L. Gao, A. Aksimentiev, Rapid and accurate determination of nanopore ionic current using a steric exclusion model. *ACS Sens.* **4**, 634–644 (2019).
67. M. Wanunu *et al.*, Rapid electronic detection of probe-specific microRNAs using thin nanopore sensors. *Nat. Nanotechnol.* **5**, 807–814 (2010).
68. M. J. Kim, M. Wanunu, D. C. Bell, A. Meller, Rapid fabrication of uniformly sized nanopores and nanopore arrays for parallel DNA analysis. *Adv. Mater.* **18**, 3149–3153 (2006).
69. S. W. Kowalczyk, A. Y. Grosberg, Y. Rabin, C. Dekker, Modeling the conductance and DNA blockade of solid-state nanopores. *Nanotechnology* **22**, 315101 (2011).